atmosphere

Communication

Climatology of Tropospheric Relative Humidity over the Korean Peninsula from Radiosonde and ECMWF Reanalysis

Hwan-Jin Song *, Sunyoung Kim, Hyesook Lee and Ki-Hoon Kim

National Institute of Meteorological Sciences, Korea Meteorological Administration, Jeju 63568, Korea; sykim80@korea.kr (S.K.); hslee05@korea.kr (H.L.); kh.kim@korea.kr (K.-H.K.)

* Correspondence: hwanjinsong@gmail.com or atmos85@korea.kr

Received: 17 June 2020; Accepted: 30 June 2020; Published: 2 July 2020

Abstract: Conventional radiosondes can be used to measure the relative humidity over liquid (RHL) by assuming a saturated vapor pressure over the liquid. However, this assumption results in significant errors with respect to measurements in the upper troposphere, where the effect of ice is dominant. Therefore, this study presents a novel method that considers the effects of ice to determine the relative humidity from radiosonde RHL data for the last 40 years (1979–2018) over the upper layers of the Korean peninsula. Even though the relative humidity obtained from the reanalysis data was significantly different from the radiosonde-based RHL, the difference was much reduced when relative humidity was calculated using the novel method proposed in this study. Such improvements in the estimated relative humidity could be attributed to the consideration of the ice effect at temperatures above freezing level. Additionally, the validity of the relative humidity estimated in this study was established based on a two-week case analysis of data from Boseong station. Furthermore, two peak relative humidity modes for the lower and upper layers were clearly identified in the mean climatology profiles, which indirectly suggested the absence of mid-level clouds around the 700-hPa level and 500-hPa level in winter and summer, respectively. This study is meaningful as it is the first study to determine the relative humidity distribution over the Korean peninsula using radiosonde observations. The scientific value obtained can potentially be expanded by applying the proposed method to other radiosonde observation networks, which are widely distributed worldwide.

Keywords: relative humidity; radiosonde; ERA-Interim; ERA5; Korea

1. Introduction

Relative humidity is a variable used to describe the amount of moisture in the atmosphere, and it is defined as the ratio of vapor pressure to saturation vapor pressure (e_s). As the Clausius-Clapeyron equation is normally used to determine e_s, the relative humidity is affected by both temperature and moisture levels. Balloon-based radiosonde (or rawinsonde) sounding is an in-situ relative humidity profile measurement technique extensively used worldwide. Typically, to improve forecasting performance, radiosonde data are used to assimilate and validate numerical weather prediction models [1–3] and to monitor long-term climate changes in the atmosphere [4,5]. Additionally, radiosonde observations have been widely used to validate data of relative humidity products from infrared and microwave remote sensing measurements [6–9]. Furthermore, radiosonde soundings have also been used as reference profiles for radiative transfer models or ideal numerical model simulations [10,11]. The radiosonde soundings can be directly compared with aircraft-based and dropsonde in-situ observations [12,13]. Since the radiosonde data are used as core observation in various observation campaigns, such as the Atmospheric

Radiation Measurement (ARM) [14], the Global Climate Observing System (GCOS) Reference Upper-Air Network (GRUAN) [15], Tropical Ocean Global Atmosphere Coupled Ocean Atmosphere Response Experiment (TOGA COARE) [16], Tropical Rainfall Measuring Mission Large-scale Biosphere–Atmosphere (TRMM-LBA) [17], Southern China Monsoon Rainfall Experiment (SCMREX) [18], research can be further expanded through synergy with other datasets during field observations.

Conventional radiosonde sensors measure the relative humidity with respect to liquid (RHL) by assuming the saturation vapor pressure above the liquid (e_{sl}). However, radiosonde observations in the upper troposphere can be significantly influenced by the surrounding environment, where ice is dominant. In particular, it is not physically appropriate to use the radiosonde RHL data measured at temperatures below −40 °C, at which the existence of supercooled liquid water is unexpected. Moreover, it is unreasonable to always calculate the relative humidity with respect to ice (RHI) at temperatures below 0 °C using the saturation vapor pressure over ice because there is a mixed-phase zone between −40 and 0 °C, wherein liquid and ice coexist. Therefore, the results of RHI studies using conventional radiosonde measurements were limited, such as in Polar areas [19,20] and cirrus clouds [21] that ice water is dominant.

Radiosonde RHL observations can be used to validate relative humidity data from numerical weather forecasting models. However, in these models, relative humidity is usually calculated by considering the mixed liquid and ice state. Therefore, if the relative humidity of the model is evaluated using the radiosonde RHL data, the model will exhibit a moisture bias in the upper troposphere, because RHI is always greater than RHL. To overcome this setback, the RHL data of the model can be compared to those obtained from radiosonde observations [22]. However, since several studies based on radiosonde or dropsonde soundings have reported the moist bias of models or dry bias of sondes, their validation methods are strongly suspected to have fundamental problems [23–31] resulting from an unfair comparison. Previous studies have also reported the correction of RHL dry bias of conventional radiosondes using an advanced sensor such as a cryogenic frost point hygrometer [32–34]. However, data from such sensors are based on special observations, and they are extremely limited regarding distribution and time. For example, Fujiwara et al. [35] used only 111 soundings of frost point hygrometer data over the tropics to analyze the period of 1993–2009. The characteristics of upper-level humidity in the Korean peninsula have not been properly understood because observation-based RHI measurements have been unavailable for that area.

Therefore, the main objective of this study is to understand the climatology of humidity profiles over the Korean peninsula using radiosonde observations in combination with reanalysis data, especially in the mixed-phase zone wherein liquid and ice coexist. For this purpose, we developed a method to estimate realistic relative humidity within the mixed-phase zone using conventional radiosonde-based RHL data. The mixed zone is the atmospheric layer with the most uncertainty in numerical weather forecasting models [36–38]. Therefore, the radiosonde-based relative humidity estimated in this study is expected to provide a deeper understanding of the mechanisms of cloud formation and precipitation [39,40], along with cloud dynamics related to ascending/descending motion and riming process related to the growth of ice particles. In particular, if this study is combined with ground-based or satellite-based cloud radar and lidar measurements, such as in [21,41,42], it could greatly contribute to understanding the cloud processes. This study also has significance for the evaluation of reanalysis humidity data using conventional radiosonde observations.

2. Data

The radiosonde database of the University of Wyoming, which is one of the most popular datasets worldwide, was used in this study to obtain radiosonde data over a period of 40 years (1979–2018). The data used included temperature and RHL profiles, and the total number of soundings was 205,133. Figure 1 shows the locations of the stations from which the radiosondes were launched at least once over the Korean peninsula, as well as the surrounding regions, including Japan. The nine stations marked with red squares indicate representative stations at which the soundings were performed over 1000 times. The soundings were obtained most frequently at the Osan station, followed by the Gwangju, Fukuoka, Pohang, Gosan, Baengnyeongdo, Sokcho, Heuksando, and Paju stations (Table 1). Among these stations, Osan and Gwangju stations had been operated by the United States Air Force and were characterized by regular observations performed four times a day (i.e., at 6-h intervals), thereby being distinguished from other stations using the conventional interval of 12 h. The use of long-term observations from multiple sources (different manufactures and sensors) could generate potential uncertainty in this study. The 1524LA sensor made by the Jinyang (South Korea) has been used most popularly for Osan and Gwangju stations operated by the Air Force, while the Korea Meteorological Administration (KMA) stations have mostly used the Jinyang 1524L before 1997, Vaisala (Finland) RS80 for 1997–2007, Vaisala RS92 (-SGP) for 2008–2011, Graw (Germany) DFM-06 for 2007–2012, Jinyang RSG-20A after 2011. Thus, the Jinyang 1524 sensors accounts for the largest portion of the data for the total 40-year period. Note that the use of old-version sensor may affect the quality of data [34,43]. For example, the Vaisaia RS80 sensor had issues with icing whereas the later version (RS92) relied on an alternate-heating method of the sensors to ensure that ice never built up and actual liquid water was measured by the radiosonde [33]. The comparison of total column water vapor with the Global Positioning System (GPS) observations showed the root mean square errors (RMSEs) of 2.09 mm for the Vaisaia RS92, 2.46 mm for the Vaisaia RS80, 2.81 mm for the Graw DFM-06 at the Sockho station over Korea [44]. Similarly, the comparison results in the water vapor column between the GPS and radiosonde observations at the Osan station (Jinyang 1524) showed better agreement (about 30% or more lower bias) compared with those in the Jeju station (Vaisala RS80), although dry bias is found in both of the sensors [45]. Recent results using the Vaisala RS92 and Jinyang RSG-20A at the Sockho station [46] exhibited much lower bias and RMSE compared with [44], while it depends on the mean temperature equation used in the GPS retrieval algorithm. Furthermore, because radiosonde-mounted balloons have the tendency to drift up to a maximum of 75 km at a 300-hPa pressure level depending on the surrounding wind velocity [47], continuous vertical sounding from a fixed location cannot be guaranteed. Nevertheless, we assumed that most errors resulting from sensors and spatial displacement were smoothed out via long-term averaging of radiosonde data.

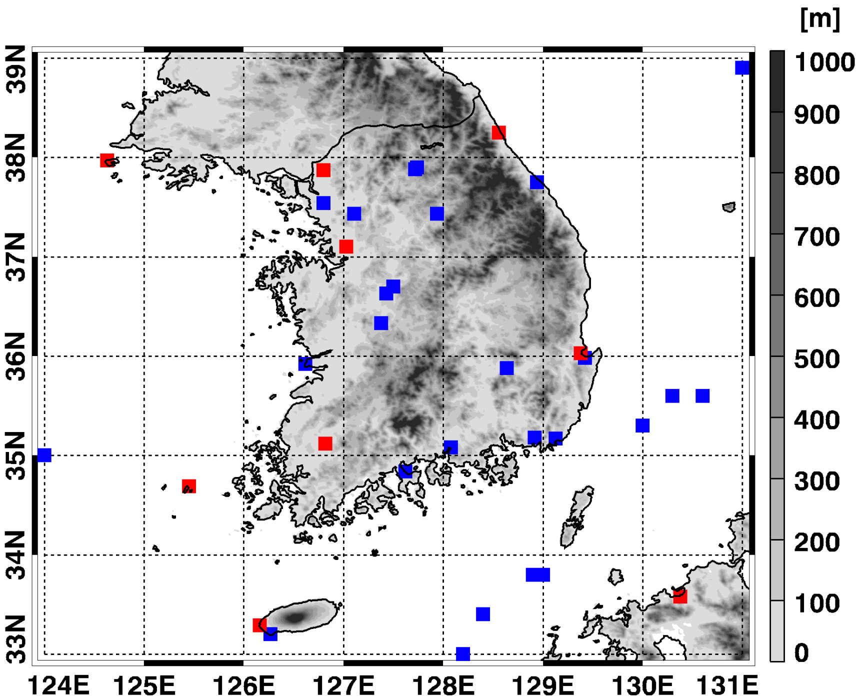

Figure 1. Location of radiosonde stations over Korea (gray contours represent topography and the red squares indicate stations from which over 1000 soundings were conducted).

Table 1. Information on radiosonde sites.

Index	Code	Station Name	Location Information	Number of Soundings
1	RKSO	Osan	37.10° N, 127.03° E, 52 m	50,303
2	RKJJ	Gwangju	35.12° N, 126.82° E, 13 m	40,584
3	47807	Fukuoka	33.58° N, 130.38° E, 15 m	33,769
4	47138	Pohang	36.03° N, 129.38° E, 6 m	28,629
5	47185	Gosan	33.29° N, 126.16° E, 73 m	20,714
6	47102	Baengnyeongdo	37.97° N, 124.63° E, 158 m	13,631
7	47090	Sokcho	38.25° N, 128.56° E, 18 m	10,743
8	47169	Heuksando	34.69° N, 125.45° E, 69 m	3843
9	RKSB	Paju	37.87° N, 126.80° E, 10 m	2381
10	JCCX	Sea	35.00° N, 124.00° E, 0 m	133
11	UWEC	Sea	38.90° N, 131.00° E, 0 m	79
12	UUPB	Sea	33.80° N, 128.90° E, 0 m	57
13	JBOA	Sea	33.00° N, 128.20° E, 0 m	56
14	JIVB	Sea	35.60° N, 130.60° E, 0 m	36
15	RKTU	Gimpo	36.70° N, 127.50° E, 58 m	26
16	47132	Daejeon	36.33° N, 127.38° E, 64 m	21
17	EREI	Sea	33.80° N, 129.00° E, 0 m	21
18	RKNN	Gangneung	37.75° N, 128.94° E, 6 m	17
19	47131	Cheongju	36.63° N, 127.43° E, 59 m	17
20	EREB	Sea	35.30° N, 130.00° E, 0 m	15
21	RKNH	Hoengsong	37.43° N, 127.94° E, 101 m	13
22	RKSS	Gimpo	37.54° N, 126.80° E, 18 m	11
23	47141	Gunsan	35.92° N, 126.62° E, 10 m	8
24	47139	Pohang2	35.98° N, 129.42° E, 20 m	5
25	47101	Chuncheon	37.90° N, 127.74° E, 78 m	4
26	RKJY	Yeosu	34.84° N, 127.62° E, 21 m	4
27	RKSM	Seongnam	37.43° N, 127.11° E, 20 m	3
28	RKTN	Daegu	35.88° N, 128.64° E, 37 m	2
29	RKPK	Kimhae	35.18° N, 128.92° E, 6 m	2
30	47104	Bukgangneung	37.88° N, 127.72° E, 76 m	1
31	UAAQ	Sea	35.60° N, 130.30° E, 0 m	1
32	47154	Busan	35.17° N, 129.13° E, 2 m	1
33	RKPS	Sacheon	35.08° N, 128.08° E, 8 m	1
34	RBOA	Sea	33.40° N, 128.40° E, 0 m	1
35	47187	Moseulpo	33.20° N, 126.27° E, 13 m	1

Liquid water content (LWC) and ice water content (IWC) profiles were obtained from the European Centre for Medium Range Weather Forecasts (ECMWF) ERA-Interim (ERAI) [1], and new high-resolution ERA5 [48] reanalysis data were used. ECMWF Reanalysis 5 (ERA5) is a new ECMWF reanalysis dataset that replaced the conventional ERAI data, and it presents improvement with respect to data assimilation, ancillary inputs, vertical levels (60 to 137 levels), horizontal grid (79 to 31 km), and temporal resolution (6 to 1 h). In this study, monthly mean temperature, relative humidity, LWC, and IWC profiles for 27 vertical pressure levels (100–1000 hPa) from ERAI and ERA5 data were used over the study domain, as shown in Figure 1. The relative humidity of the reanalysis data represents realistic humidity because model considers a mixture of RHL and RHI. To fairly compare the reanalysis data-based RHL with that obtained from the radiosonde observations, temperature and specific humidity data collected at 6-h intervals were also used to calculate the reanalysis data-based RHL.

As a case analysis, this study used raw data from radiosonde observations (Vaisala RS92 and RS92-SGP) collected at 3-h intervals at Boseong station (34.7633° N, 127.3123° E), between 06:00 UTC 2 July 2018 and 09:00 UTC 17 July 2018. The corresponding observation case was selected based on continuous observations with relatively high temporal resolution (3 h). The raw radiosonde data presented a high vertical resolution, with 0.01 km intervals for a 0–17 km range. The cloud fraction and cloud (liquid + ice) water content profiles from the ECMWF reanalysis datasets were further used with the same 3-h intervals.

3. Method

There are several formulas to determine saturation vapor pressure over liquid (e_{sl}) and over ice (e_{si}). Therefore, different values might be obtained for these parameters. However, this is not the issue addressed here. This study uses the formulas for e_{sl} and e_{si} suggested by [49], which has been operationally used in ECMWF reanalyses [1,50]. The calculations were conducted using a hybrid method (suggested by [49]) that combines e_{sl} and e_{si} to calculate e_s in a mixed temperature zone between −23 and 0 °C (e_{sl} above 0 °C and e_{si} below −23 °C were used).

As shown in Figure 2, at temperatures below 0 °C, e_{si} is always smaller than e_{sl}, and their ratio (e_{sl}/e_{si}) increases linearly as the temperature decreases. For instance, the e_{sl}/e_{si} ratio increased from 121% at −20 °C to 146% at −40 °C. Given that e_s was used as the denominator in the calculation of relative humidity; this difference was directly associated with the uncertainty of relative humidity. Figure 2b shows the monthly climatology of the ERAI ratio of LWC to the total water content (i.e., liquid water fraction) over Korea. Between winter and summer (June–August), the liquid water fraction clearly increased, owing to the temperature rise. In summer, the liquid water fraction was approximately 50% at approximately 500 hPa because the difference between e_{sl} and e_{si} at −1 °C is only 0.1%, as shown in Figure 2a. The realistic expression of relative humidity was almost possible despite the use of e_{sl} for the corresponding layer. However, RHL no longer represents a realistic state because in summer the liquid water fraction is only 10% at pressures lower than 400 hPa, and in winter, when the temperature drops, the uncertainty of RHL increases even more owing to the decrease in the liquid water fraction.

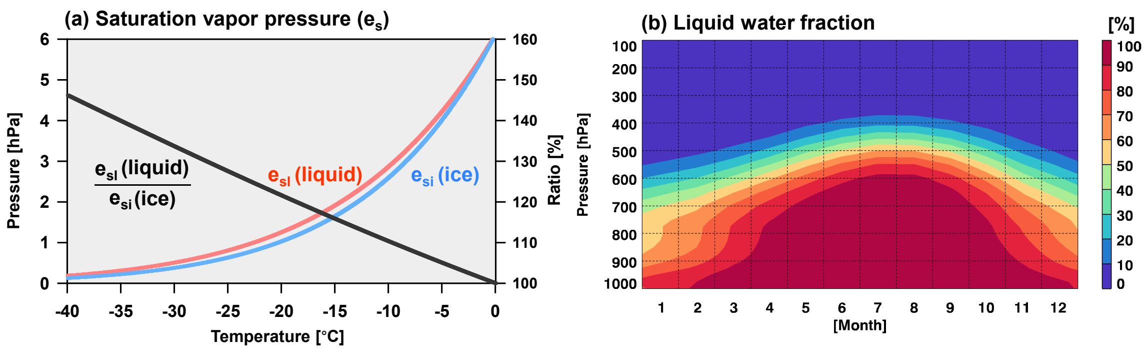

Figure 2. (**a**) Saturation vapor pressures over liquid and ice (e_{sl} and e_{si}). (**b**) Monthly climatology for Table 1. RHL was applied for temperatures ≥ 0 °C (Equation (2)), whereas RHI was used for temperatures < −23 °C (Equation (3)). For temperatures between −23 °C and 0 °C, Equation (4) was used to estimate relative humidity.

Even though the RHI equation was applied for temperature (T) < −23 °C, the RHL error at the upper layer, which presents a temperature below −23 °C, was inevitably large because the raw radiosonde observation RHL data were derived by assuming saturated vapor pressure over liquid water. Furthermore, regarding the measurement uncertainty, radiosondes generally record RHL in units of 1%. Therefore, the error can be large because relative humidity is mostly determined using temperature data only. Lastly, an empirical correction (for temperatures below 0 °C) was performed based on a linear-regression analysis between monthly liquid water fraction (LWF) profiles and the difference between ERAI- and radiosonde-based relative humidity (Equation (6)). This correction further improves the determination of the radiosonde-based relative humidity. Here, we did not allow more than 100% relative humidity. If the supersaturated air is considered in the future study, it would be beneficial to understand the complex cloud process. In conclusion, the equations used to estimate relative humidity (RH) were as follows:

$$e = e_{sl} \times RHL/100 \tag{1}$$

$$e_s(T) = e_{sl}(T) = 6.114\exp[17.502 \times (T - 273.16)/(T - 32.19)],\ T \geq 273.16\ K \tag{2}$$

$$e_s(T) = e_{sl}(T) = 6.114\exp[22.587 \times (T - 273.16)/(T + 0.7)],\ T < -23 + 273.16\ K \tag{3}$$

$$e_s(T) = e_{si}(T) + [e_{sl}(T) - e_{si}(T)] \times [(T + 23 - 273.16)/23]^2, -23 + 273.16\ K \leq T < 273.16\ K \tag{4}$$

$$RH = e/e_s \times 100\ (\%) \tag{5}$$

$$RH_{new} = RH \times (1.10870 - 0.000603942 \times LWF),\ T < 273.16\ K \tag{6}$$

There are two main assumptions in this approach. The first one is the combination method between e_{sl} and e_{si} in the mixed phased zone proposed by [49], especially for the cut off at −23 °C. The e_s in the actual situation may not be elaborately expressed in Equation (4), and thus it can cause the overestimation or underestimation of RH. Second is the empirical correction based on the climatological relationship between LWF and the RH difference. These assumptions can lead to some errors. For example, real cloud conditions may differ from the obtained values when liquid clouds rise upward owing to deep convection, or when ice clouds descend to lower layers owing to the strong downdraft and cold air inflow in the upper layers. The former and latter phenomena can lead to the underestimation and overestimation of relative humidity, respectively. Nevertheless, the results are meaningful as this is a novel research on this topic because it is one of the first extensive studies to look at the relative humidity over the Korean peninsula and provides a moisture climatology using the conventional radiosonde observations. Note that dry bias correction was not performed in this study owing to the radiative heating during the daytime [34,51–53] and characteristics of polymeric thin-film humidity sensor itself [54,55], and thus this issue may have a significant effect on the results of the study. If the radiosonde measurements were actually observed in the dry-bias situation the RHI enhancement attempted in this study may be somewhat excessive.

4. Results

In Figure 3, the temperature, RHL, and relative humidity profiles of ERAI and radiosonde datasets are compared. With respect to temperature, both datasets showed typical patterns in which the temperature in the upper layers rises in summer and drops in winter (Figure 3a,b). In both datasets, the tropopause presented the lowest temperature pattern. Considering the consistency of the two temperature datasets, the bias and RMSE were −0.12 and 0.45 °C, respectively, for all atmospheric layers. Particularly, the mean bias was observed at a level of 0.1 °C, which is the measurement unit of radiosondes. In summer, the freezing and −40 °C levels (supercooled liquid water cannot exist above the −40 °C level) were approximately 500 and 250 hPa, and in winter, they both dropped to 700 and 350 hPa, respectively. The temperature difference between the two datasets was small, indicating that it cannot explain large relative humidity discrepancies between radiosonde and reanalysis data (shown in Figure 3f,i). However, the negative bias was mostly at altitudes of 200–700 hPa in regions of significant cloud cover (Figure 3c). The thermodynamic processes within clouds represented by the reanalysis products might be leading to this potential cold bias and may be worth exploring in future research.

A common characteristic of both ERAI and radiosonde datasets is that they presented a large RHL value in summer (Figure 3d,e). Furthermore, the consistency of the ERAI- and radiosonde-based RHL values was remarkably high in the middle to low troposphere. In the ERAI dataset, the maximum altitude for RHL above 40% was approximately 200 hPa, whereas in the radiosonde dataset, it was limited to 350 hPa, thereby indicating that the radiosonde dataset consistently underestimates RHL for those levels. This feature was reversed, resulting in the overestimation of the radiosonde RHL value above the 200-hPa level. These are clearly shown in the difference of RHL between the two datasets (Figure 3f). However, the reliability of the RHL observed at temperatures below −40 °C was likely inaccurate in connection with the problems presented in previous study [34,48–52]. Moreover, the radiosonde RHL measurements were slightly higher than those obtained from the ERAI dataset at altitudes corresponding to 400–800 hPa in the cold seasons (Figure 3f). However, the higher near-surface RHL values in the ERAI during the cold seasons compared with that in the radiosonde (Figure 3f) are interpreted as the results of artificial extrapolation of the ERAI to the 1000 hPa level over the land area in addition to the contrast between ocean and land (i.e., more humid condition over the ocean). The bias of the ERAI-based RHL was 1.28% and its RMSE was 4.27% compared to the radiosonde-based RHL for the temperature range from −40 °C to 0 °C, while the ERA5-based RHL showed a bias of 0.07% and an RMSE of 4.83%. The ERA5 temperature data also showed lower simulation performance compared to the ERAI temperature data (bias = −0.20 °C, and RMSE = 1.61 °C). The fundamental cause of this lower performance is still unclear, but it possibly resulted from a regional characteristic specific to the Korean peninsula. Therefore, the climatological analyses in this study were mainly performed using the ERAI data.

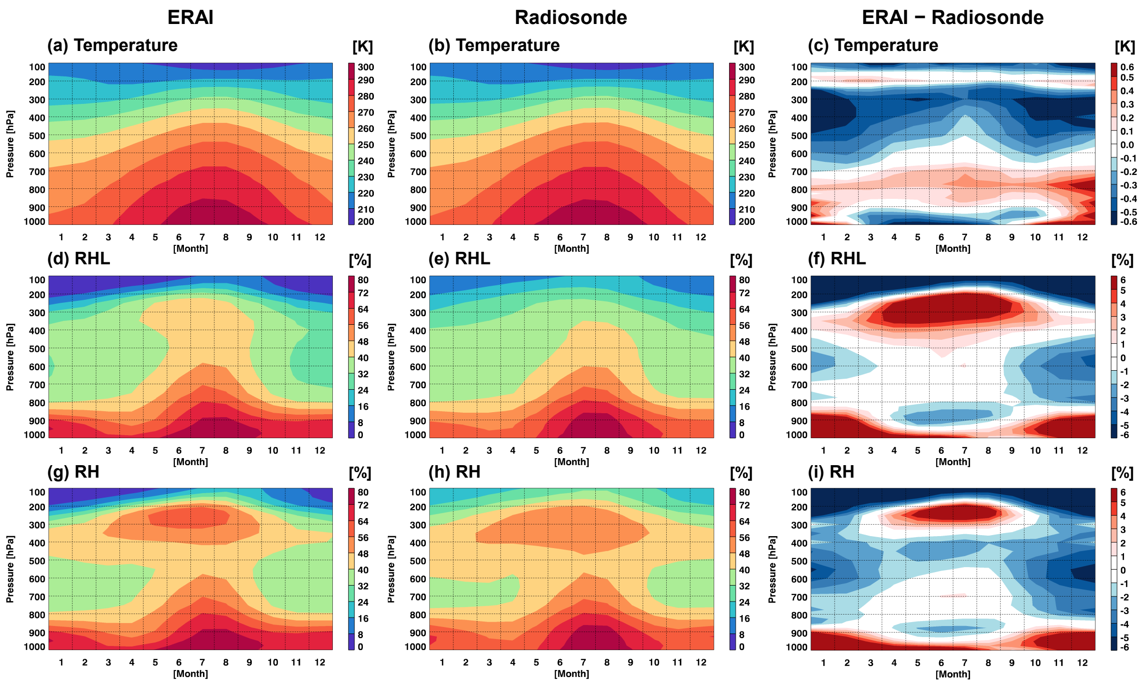

Figure 3. Monthly climatology profiles of (**a**,**b**) temperature, (**d**,**e**) relative humidity with respect to liquid (RHL), and (**g**,**h**) relative humidity with respect to ice (RHI) based on ERAI (left) and radiosonde (middle) datasets. The differences between ERA-Interim (ERAI) and radiosonde data are given in the right panel (**c**,**f**,**i**). The X-axis denotes each month from January to December.

Figure 3g shows the mean climatology of the operational ERAI-based RH products, which were obtained by considering the liquid and ice mixed state. If this was not considered and a direct comparison with the radiosonde-based RHL were made, as shown in Figure 3e, an incorrect conclusion could be made that the relative humidity in the reanalysis or model data was highly overestimated compared to that of the radiosonde observations. The mean difference between the ERAI-based relative humidity and the radiosonde-based RHL between −40 and 0 °C levels was 5.18 ± 6.63% (bias ± standard deviation). Figure 3h, which is physically equivalent to Figure 3g, shows the newly calculated relative humidity distribution. The RH shown in Figure 3h indicates an enhancement compared to the RHL shown in Figure 3e at altitudes above the 0 °C level, and the degree of enhancement was proportional to the decrease in temperature and the fraction of ice. As shown in Figure 3h, the relative humidity enhancement above 40% was confirmed at 200–600 hPa. Such a relative humidity enhancement contributes significantly to the radiosonde-based relative humidity, with a distribution similar to that of the ERAI-based relative humidity. In radiosonde RHL-based studies, it is difficult to identify the peak relative humidity mode in the upper troposphere because the RHL tends to decrease with increasing altitude [24,27]. In the present study, the two peak relative humidity modes were identified in the lower and upper layers. It is scientifically meaningful because it indirectly suggests the relative absence of mid-level relative humidity (or clouds) around the 700 hPa level in winter and 500 hPa level in summer. The ERAI-based relative humidity showed a mean difference of −1.31 ± 3.06% compared to the radiosonde-based relative humidity (Figure 3g,h). The RMSEs and pattern correlations were also significantly improved, from 8.39% and 0.726 (ERAI RH − Radiosonde RHL) to 3.32% and 0.974 (ERAI − Radiosonde RH) for −40 and 0 °C levels, respectively. In particular, the positive differences at 200–400 hPa levels in the warm season were much reduced in the RH (Figure 3i) compared to the RHL (Figure 3f). Additionally, the relative humidity estimated using the ERA5 data showed a higher RMSE (3.85%) and lower pattern correction (0.956) compared to those obtained in this study.

Figure 4 shows the temperature, RHL, and relative humidity profiles during the intensive observation periods performed in July 2018 at Boseong station. Relative humidity is often used to directly parameterize the cloud fraction [56]. For the radiosonde-based RHL, deep convection occurred three times between 3 and 6 July, as shown in Figure 4a. On 9 July, middle-level clouds were observed and, thereafter, clear sky conditions with high-level cirrus clouds (until 13 July) prevailed. These can be confirmed by the ECMWF reanalysis cloud products (Figure 5). Note that if cloud radar measurements were available, a more accurate diagnosis of cloud profiles would have been possible, as in [21]. The temperature distributions between the radiosonde and ECMWF reanalysis data were almost similar, although the low-resolution ECMWF reanalysis data did not accurately represent the small-scale disturbance (Figure 4a,d,g).

The ERAI- and ERA5-based RHLs displayed temporal and vertical changes (Figure 4e,h) similar to those found in observations. However, the relative humidity distribution reveals new results that were overlooked in the RHL distribution. When the peak height corresponding to a relative humidity greater than 90% was considered the cloud top, between 3 and 6 July, the cloud-top height in the RHL results was estimated at approximately 400 hPa. However, a deep convection reaching 200 hPa was observed in the relative humidity results, as shown in Figures 4c and 5. Similar features were also identified in the ERAI and ERA5 relative humidity results (Figure 4f,i). Throughout the analysis period, the temperatures of −40 and 0 °C, which corresponded to 250 and 500 hPa, respectively, remained almost uniform (Figure 4a,d,g). Therefore, the new relative humidity obtained in this study for 250–500 hPa was a more realistic representation of the cloud-top heights, compared to those based on the conventional RHL method.

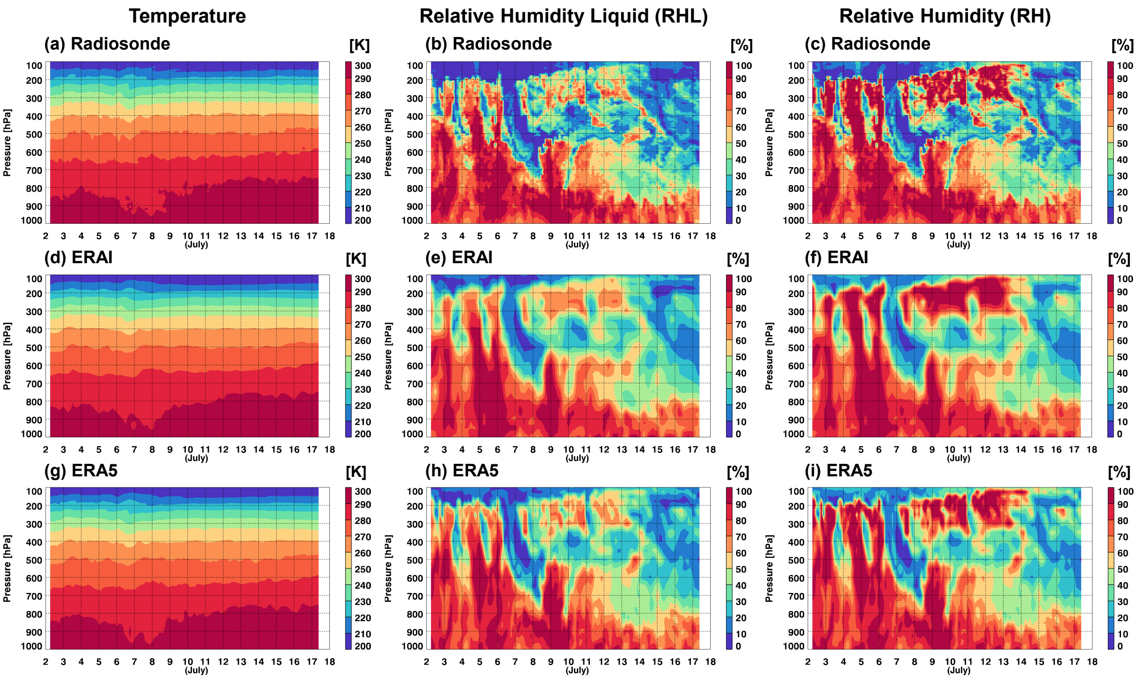

Figure 4. Time series of profiles of temperature (left), relative humidity with respect to liquid (middle), and relative humidity (right) based on (**a**–**c**) radiosonde, (**d**–**f**) ERAI, and (**g**–**i**) ECMWF Reanalysis 5 (ERA5) datasets at the Boseong station in July 2018.

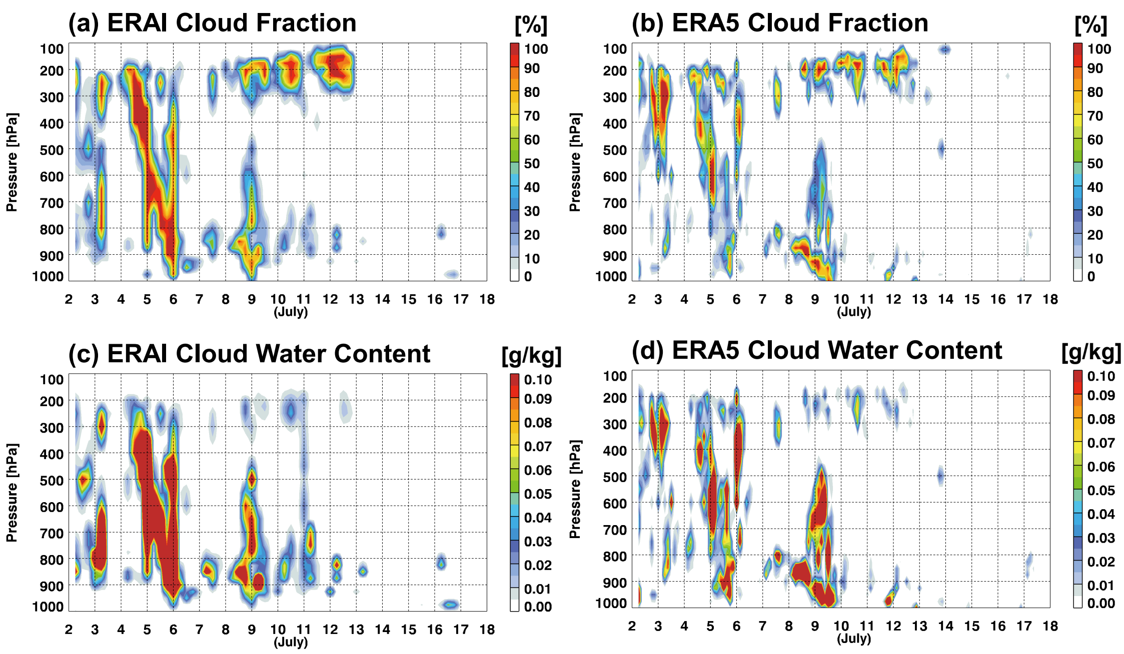

Figure 5. Time series of profiles of cloud fraction and cloud (liquid + ice) water content (bottom) for ERAI and ERA5 datasets at the Boseong station in July 2018: (**a**) Cloud fraction for ERAI dataset; (**b**) cloud fraction for ERA5 dataset; (**c**) cloud water content for ERAI dataset; (**d**) cloud water content for ERA5 dataset.

The method developed can show a continuous relative humidity distribution for layers with temperatures less than −40 °C, in the range −40 °C to 0 °C, and above 0 °C. Moreover, the upper layer clouds that were observed at 100–350 hPa between 7 and 13 July were more distinct in the relative humidity results than in the RHL results (Figure 4c). This pattern is consistent with the reanalysis results shown in Figure 4f,i. Compared to the radiosonde-based relative humidity observations, the ERAI and ERA5 datasets showed mean errors of 0.54 ± 16.60% and 0.28 ± 14.53%, respectively, for temperatures between −40 and 0 °C. The RMSEs and pattern correlations were 16.60% and 0.85 for the ERAI, but 14.52% and 0.89 for the ERA5, respectively. Therefore, the radiosonde-based relative humidity was more consistent with the high-resolution ERA5 results in this case. The reduced differences in the ERA5 can be clearly identified in Figure 6. A greater portion of the positive bias was due to the errors in the original RHL dataset (3.33 ± 13.99%, 3.06 ± 12.39%). However, the reanalysis data were limited with respect to the accuracy of the relative humidity simulation of a particular position at 3-h intervals.

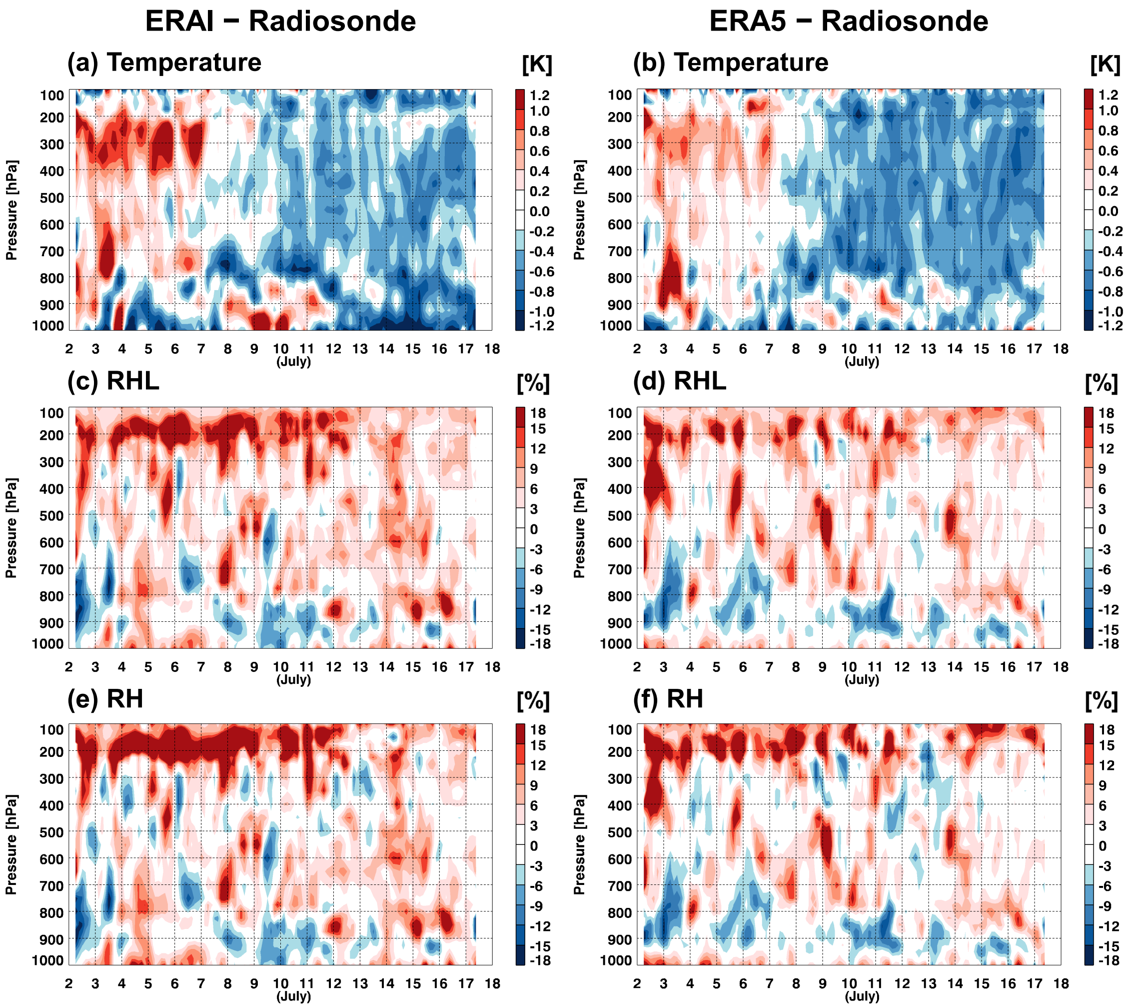

Figure 6. Same as Figure 4, but for the ERAI—Radiosonde (**a**,**c**,**e**) and ERA5—Radiosonde (**b**,**d**,**e**).

Although this study investigated the Korean peninsula, the proposed method can be applied anywhere to estimate relative humidity profiles using RHL data from conventional radiosonde data, which have been widely distributed worldwide for a long time. To apply this study to other regions, no special preparation is needed if only the method proposed by [46] is used. Furthermore, because the reanalysis data cover the world, it is also possible to compare observation-based estimation and reanalysis products in terms of relative humidity profiles. Further considering the liquid water fraction profiles, this information should be updated locally. Similar but different forms of empirical correction may also be possible. Since this is the first known study to estimate relative humidity using RHL from conventional radiosonde soundings, it is expected to have a wide range of applications.

5. Summary and Conclusions

The RHL data from radiosonde observations have a fundamental problem, as the saturation vapor pressure over liquid is applied even in the upper troposphere, where is dominated by ice. This greatly restricts the use of upper-level humidity for radiosonde data. In this study, a novel relative humidity calculation method based on conventional radiosonde RHL data was developed, and the algorithm was constructed for the mixed-phase zone in the upper troposphere. Considering 40 years (1979–2018) of climatology data over the Korean peninsula, the ERAI-based relative humidity presented a difference of 5.18 ± 6.63% and a RMSE of 8.39% compared to the radiosonde-based RHL. Compared to radiosonde observations, several previous studies have reported the moisture bias of such models. However, such systemic bias may result from physically inconsistent comparison. When the ERAI-based RH was compared to the relative humidity calculated in this study, the difference and RMSE were −1.31 ± 3.06% and 3.32%, respectively. The pattern correlations of RH distribution were also significantly improved from 0.726 to 0.974. These improvements were mainly attributed to the further consideration of the RHI effect above freezing level. In this study, two peak relative humidity modes for the lower and upper layers of the mean climatology profiles were interestingly identified, thereby indirectly suggesting the absence of mid-level clouds around the 700 hPa and 500 hPa in winter and summer, respectively. The validity of the relative humidity estimated in this study was confirmed based on the two-week case analysis at Boseong station. The results indicate that more realistic and vertically continuous monitoring can be facilitated using the relative humidity calculation method developed.

The significance of this research is highlighted by the description of relative humidity climatology based on radiosonde observations over the Korean peninsula and the comparison of results with reanalysis data. Although only the Korean peninsula was analyzed, the proposed method can be applied to other regions. Therefore, the results presented in this paper provide a basis for further insights for the expansion of radiosonde sounding applications. This expansion, in turn, could advance our understanding of moisture and cloud processes in the mixed-phase zone.

Funding: This work was funded by the KMA Research and Development Program "Development of the AI technique for the prediction of rainfall optimized over the Korean peninsula" under Grant (KMA2018-00124).

Acknowledgments: The authors thank anonymous reviewers for constructive and variable comments. We also thank Young-Chan Noh (CIMSS) for providing inspiration for this study. The radiosonde soundings used in this study were obtained from the University of Wyoming (http://weather.uwyo.edu/upperair/sounding.html). The ERAI and ERA5 reanalysis data were downloaded from http://apps.ecmwf.int/datasets/data/interim-full-daily and https://cds.climate.copernicus.eu, respectively.

Conflicts of Interest: The authors declare no conflict of interest.

References

1. Dee, D.P.; Uppala, S.M.; Simmons, A.J.; Berrisford, P.; Poli, P.; Kobayashi, S.; Andrae, U.; Balmaseda, M.A.; Balsamo, G.; Bauer, P.; et al. The ERA-Interim reanalysis: Configuration and performance of the data assimilation system. *Q. J. R. Meteorol. Soc.* **2011**, *137*, 553–597. [CrossRef]
2. Hong, S.-Y.; Kwon, Y.C.; Kim, T.-H.; Kim, J.-E.E.; Choi, S.-J.; Kwon, I.-H.; Kim, J.; Lee, E.-H.; Park, R.-S.; Kim, D.-I. The Korean Integrated Model (KIM) system for global weather forecasting. *Asia-Pac. J. Atmos. Sci.* **2018**, *54*, 267–292. [CrossRef]
3. Walters, D.; Baran, A.J.; Boutle, I.; Brooks, M.; Earnshaw, P.; Edwards, J.; Furtado, K.; Hill, P.; Lock, A.; Manners, J.; et al. The Met Office Unified Model Global Atmosphere 7.0/7.1 and JULES Global Land 7.0 configurations. *Geosci. Model Dev.* **2019**, *12*, 1909–1963. [CrossRef]
4. Dai, A.; Wang, J.; Thorne, P.W.; Parker, D.E.; Haimberger, L.; Wang, X.L. A new approach to homogenize radiosonde humidity data. *J. Clim.* **2011**, *24*, 965–991. [CrossRef]
5. Maturilli, M.; Kayser, M. Arctic warming, moisture increase and circulation changes observed in the Ny-Ålesund homogenized radiosonde record. *Theor. Appl. Climatol.* **2017**, *130*, 1–17. [CrossRef]

6. Liljegren, J.; Boukabara, S.-A.; Cady-Pereira, K.; Clough, S.A. The effect of the half-width of the 22-GHz water vapor line on retrievals of temperature and water vapor profiles with a twelve-channel microwave radiometer. *IEEE Trans. Geosci. Remote Sens.* **2005**, *43*, 1102–1108. [CrossRef]
7. Tobin, D.C.; Revercomb, H.E.; Knuteson, R.O.; Lesht, B.M.; Strow, L.L.; Hannon, S.E.; Feltz, W.F.; Moy, L.A.; Fetzer, E.J.; Cress, T.S. Atmospheric Radiation Measurement site atmospheric state best estimates for Atmospheric Infrared Sounder temperature and water vapor retrieval validation. *J. Geophys. Res.* **2006**, *111*, D09S14. [CrossRef]
8. Miloshevich, L.M.; Vo¨mel, H.; Whiteman, D.N.; Lesht, B.M.; Schmidlin, F.J.; Russo, F. Absolute accuracy of water vapor measurements from six operational radiosonde types launched during AWEX-G and implications for AIRS validation. *J. Geophys. Res.* **2006**, *111*, D09S10. [CrossRef]
9. Sun, B.; Reale, A.; Tilley, F.H.; Pettey, M.E.; Nalli, N.R.; Barnet, C.D. Assessment of NUCAPS S-NPP CrIS/ATMS sounding products using reference and conventional radiosonde observations. *IEEE J. Sel. Top. Appl. Earth Obs. Remote Sens.* **2017**, *10*, 2499–2509. [CrossRef]
10. Chevallier, F.; Chéruy, F.; Scott, N.A.; Chédin, A. A neural network approach for a fast and accurate computation of longwave radiative budget. *J. Appl. Meteorol.* **1998**, *37*, 1385–1397. [CrossRef]
11. Song, H.-J.; Sohn, B.-J.; Hong, S.-Y.; Hashino, T. Idealized numerical experiments on the microphysical evolution of warm-type heavy rainfall. *J. Geophys. Res. Atmos.* **2017**, *122*, 1685–1699. [CrossRef]
12. Vance, A.K.; Taylor, J.P.; Hewison, T.J.; Elms, J. Comparison of in situ humidity data from aircraft, dropsonde, and radiosonde. *J. Atmos. Ocean. Technol.* **2004**, *21*, 921–932. [CrossRef]
13. Soddell, J.R.; McGuffie, K.; Holland, G.J. Intercomparison of atmospheric soundings from the aerosonde and radiosonde. *J. Appl. Meteorol.* **2004**, *43*, 1260–1269. [CrossRef]
14. Stokes, G.M.; Schwartz, S.E. The Atmospheric Radiation Measurement (ARM) program: Programmatic background and design of the cloud and radiation test bed. *Bull. Am. Meteorol. Soc.* **1994**, *75*, 1201–1221. [CrossRef]
15. Bodeker, G.E.; Bojinski, S.; Cimini, D.; Dirksen, R.J.; Haeffelin, M.; Hannigan, J.W.; Hurst, D.F.; Leblanc, T.; Madonna, F.; Maturilli, M.; et al. Reference upper-air observations for climate: From concept to reality. *Bull. Am. Meteorol. Soc.* **2016**, *97*, 123–135. [CrossRef]
16. Webster, P.J.; Lukas, R. The Coupled Ocean–Atmosphere Response Experiment. *Bull. Am. Meteorol. Soc.* **1992**, *73*, 1377–1416. [CrossRef]
17. Halverson, J.B.; Rickenbach, R.; Roy, B.; Pierce, H.; Williams, E. Environmental characteristics of convective systems during TRMM LBA. *Mon. Weather Rev.* **2002**, *130*, 1493–1509. [CrossRef]
18. Luo, Y.; Zhang, R.; Wan, Q.; Wang, B.; Wong, W.K.; Hu, Z.; Jou, B.J.-D.; Lin, Y.; Johnson, R.H.; Chang, C.-P.; et al. The Southern China Monsoon Rainfall Experiment (SCMREX). *Bull. Am. Meteorol. Soc.* **2017**, *98*, 999–1013. [CrossRef]
19. Gettelman, A.; Walden, V.P.; Miloshevich, L.M.; Roth, W.L.; Halter, B. Relative humidity over Antarctica from radiosondes, satellites, and a general circulation model. *J. Geophys. Res.* **2006**, *111*, D09S13. [CrossRef]
20. Treffeisen, R.; Krejci, R.; Ström, J.; Engvall, A.C.; Herber, A.; Thomason, L. Humidity observations in the Arctic troposphere over Ny-Ålesund, Svalbard based on 15 years of radiosonde data. *Atmos. Chem. Phys.* **2007**, *7*, 2721–2732. [CrossRef]
21. Dzambo, A.M.; Turner, D.D. Characterizing relative humidity with respect to ice in midlatitude cirrus clouds as a function of atmospheric state. *J. Geophys. Res. Atmos.* **2016**, *121*, 12253–12269. [CrossRef]
22. Noh, Y.-C.; Sohn, B.-J.; Kim, Y.; Joo, S.; Bell, W. Evaluation of temperature and humidity profiles of Unified Model and ECMWF analysis using GRAUAN radiosonde observations. *Atmosphere* **2016**, *7*, 94. [CrossRef]
23. Lang, R.; Lawrence, M.G. Improvement of the vertical humidity distribution in the chemistry transport model MATCH through increased evaporation of convective precipitation. *Geophys. Res. Lett.* **2005**, *32*, L17812. [CrossRef]
24. Milton, S.F.; Earnshaw, P. Evaluation of surface water and energy cycles in the Met Office global NWP model using CEOP data. *J. Meteorol. Soc. Jpn.* **2007**, *85A*, 43–72. [CrossRef]
25. Agustí-Panareda, A.; Vasiljevic, D.; Beljaars, A.; Bock, O.; Guichard, F.; Nuret, M.; Garcia Mendez, A.; Andersson, E.; Bechtold, P.; Fink, A.; et al. Radiosonde humidity bias correction over the West African region for the special AMMA reanalysis at ECMWF. *Q. J. R. Meteorol. Soc.* **2009**, *135*, 595–617. [CrossRef]
26. Faccani, C.; Rabier, F.; Fourrié, N.; Agusti-Panareda, A.; Karbou, F.; Moll, P.; Lafore, J.-P.; Nuret, M.; Hdidou, F.; Bock, O. The impact of the AMMA radiosonde data on the French global assimilation and forecast system. *Weather Forecast.* **2009**, *24*, 1268–1286. [CrossRef]

27. Kennedy, A.D.; Dong, X.; Xi, B.; Xie, S.; Zhang, Y.; Chen, J. A comparison of MERRA and NARR reanalyses with the DOE ARM SGP data. *J. Clim.* **2011**, *24*, 4541–4557. [CrossRef]
28. Feng, Y.; Cadeddu, M.; Kotamarthi, V.R.; Renju, R.; Raju, C.S. Humidity bias and effect on simulated aerosol optical properties during the Ganges Valley Experiment. *Curr. Sci.* **2016**, *111*, 93–100. [CrossRef]
29. Yang, Y.; Moore, S.; Uddstrom, M.; Turner, R.; Carey-Smith, T. Model moist bias in the middle and upper troposphere during DEEPWAVE. *Atmos. Sci. Lett.* **2017**, *18*, 161–167. [CrossRef]
30. Wang, H.; Burleyson, C.D.; Ma, P.-L.; Fast, J.D.; Rasch, P.J. Using the Atmospheric Radiation Measurement (ARM) datasets to evaluate climate models in simulating diurnal and seasonal variations of tropical clouds. *J. Clim.* **2018**, *31*, 3301–3325. [CrossRef]
31. Pante, G.; Knippertz, P. Resolving Sahelian thunderstorms improves mid-latitude weather forecasts. *Nat. Commun.* **2019**, *10*, 3487. [CrossRef] [PubMed]
32. Miloshevich, L.M.; Paukkunen, A.; Vömel, H.; Oltmans, S.J. Development and validation of a time-lag correction for Vaisala radiosonde humidity measurements. *J. Atmos. Ocean. Technol.* **2004**, *21*, 1305–1327. [CrossRef]
33. Miloshevich, L.M.; Vo¨mel, H.; Whiteman, D.N.; Leblanc, T. Accuracy assessment and correction of Vaisala RS92 radiosonde water vapor measurements. *J. Geophys. Res.* **2009**, *114*, D11305. [CrossRef]
34. Vömel, H.; Selkirk, H.; Miloshevich, L.; Valverde-Canossa, J.; Valdés, J.; Kyrö, E.; Kivi, R.; Stolz, W.; Peng, G.; Diaz, J.A. Radiation dry bias of the Vaisala RS92 humidity sensor. *J. Atmos. Ocean. Technol.* **2007**, *24*, 953–963. [CrossRef]
35. Fujiwara, M.; Vömel, H.; Hasebe, F.; Shiotani, M.; Ogino, S.-Y.; Iwasaki, S.; Nishi, N.; Shibata, T.; Shimizu, K.; Nishimoto, E.; et al. Seasonal to decadal variations of water vapor in the tropical lower stratosphere observed with balloon-borne cryogenic frost point hygrometers. *J. Geophys. Res.* **2010**, *115*, D18304. [CrossRef]
36. Franklin, C.N.; Protat, A.; Leroy, D.; Fontaine, E. Controls on phase composition and ice water content in a convection-permitting model simulation of a tropical mesoscale convective system. *Atmos. Chem. Phys.* **2016**, *16*, 8767–8789. [CrossRef]
37. Song, H.-J.; Sohn, B.-J. An evaluation of WRF microphysics schemes for simulating the warm-type heavy rain over the Korean peninsula. *Asia-Pac. J. Atmos. Sci.* **2018**, *54*, 1–12. [CrossRef]
38. Song, H.-J.; Lim, B.; Joo, S. Evaluation of rainfall forecast with heavy rain types in the high-resolution Unified Model over South Korea. *Weather Forecast.* **2019**, *34*, 1277–1293. [CrossRef]
39. Masunaga, H. Short-term versus climatological relationship between precipitation and tropospheric humidity. *J. Clim.* **2012**, *25*, 7983–7990. [CrossRef]
40. Song, H.-J.; Sohn, B.-J. Two heavy rainfall types over the Korean peninsula in the humid East Asian summer environment: A satellite observation study. *Mon. Weather Rev.* **2015**, *143*, 363–382. [CrossRef]
41. Deng, M.; Mace, G.G.; Wang, Z. Anvil productivities of tropical deep convective clusters and their regional differences. *J. Atmos. Sci.* **2016**, *73*, 3467–3487. [CrossRef]
42. Cesana, G.; Chepfer, H.; Winker, D.; Getzewich, B.; Cai, X.; Jourdan, O.; Mioche, G.; Okamoto, H.; Hagihara, Y.; Noel, V.; et al. Using in situ airborne measurements to evaluate three cloud phase products derived from CALIPSO. *J. Geophys. Res. Atmos.* **2016**, *121*, 5788–5808. [CrossRef]
43. Jensen, M.P.; Holdridge, D.J.; Survo, P.; Lehtinen, R.; Baxter, S.; Toto, T.; Johnson, K.L. Comparison of Vaisala radiosondes RS41 and RS92 at the ARM Southern Great Plains site. *Atmos. Meas. Tech.* **2016**, *9*, 3115–3129. [CrossRef]
44. Park, C.G.; Roh, K.M.; Cho, J.H. Radiosonde sensors bias in precipitable water vapor from comparisons with Global Positioning System measurements. *J. Astron. Space Sci.* **2012**, *29*, 295–303. [CrossRef]
45. Kwon, H.T.; Iwabuchi, T.; Lim, G.H. Comparison of precipitable water derived from ground-based GPS measurements with radiosonde observations over the Korean peninsula. *J. Meteorol. Soc. Jpn.* **2007**, *85*, 733–746. [CrossRef]
46. Park, H.-E.; Yoo, S.-M.; Yoon, H.S.; Chung, J.-K.; Cho, J. Performance analysis of mapping functions and mean temperature equations for GNSS precipitable water vapor in the Korean peninsula. *J. Posit. Navig. Tim.* **2016**, *5*, 75–85. [CrossRef]
47. Seidel, D.J.; Sun, B.; Pettey, M.; Reale, A. Global radiosonde balloon drift statistics. *J. Geophys. Res.* **2011**, *116*, D07102. [CrossRef]
48. Hersbach, H.; Dee, D. ERA5 reanalysis is in production. In *ECMWF Newsletter*; ECMWF: Reading, UK, 2016; Volume 147.

49. Simmons, A.J.; Untch, A.; Jakob, C.; Kållberg, P.; Und'en, P. Stratospheric water vapour and tropical tropopause temperatures in ECMWF analyses and multi-year simulations. *Q. J. R. Meteorol. Soc.* **1999**, *125*, 353–386. [CrossRef]
50. Tompkins, A.M.; Gierens, K.; Rädel, G. Ice supersaturation in the ECMWF integrated forecast system. *Q. J. R. Meteorol. Soc.* **2007**, *133*, 53–63. [CrossRef]
51. Wang, J.; Zhang, L.; Dai, A.; Immler, F.; Sommer, M.; Vömel, H. Radiation dry bias correction of Vaisala RS92 humidity data and its impacts on historical radiosonde data. *J. Atmos. Ocean. Technol.* **2013**, *30*, 197–214. [CrossRef]
52. Dzambo, A.M.; Turner, D.D.; Mlawer, E.J. Evaluation of two Vaisala RS92 radiosonde solar radiative dry bias correction algorithms. *Atmos. Meas. Tech.* **2016**, *9*, 1613–1626. [CrossRef]
53. Turner, D.D.; Lesht, B.M.; Clough, S.A.; Liljegren, J.C.; Revercomb, H.E.; Tobin, D.C. Dry bias and variability in Vaisala RS80-H radiosondes: The ARM experience. *J. Atmos. Ocean. Technol.* **2003**, *20*, 117–132. [CrossRef]
54. Choi, B.I.; Lee, S.W.; Woo, S.B.; Kim, J.C.; Kim, Y.-G.; Yang, S.G. Evaluation of radiosonde humidity sensors at low temperature using ultralow-temperature humidity chamber. *Adv. Sci. Res.* **2018**, *15*, 207–212. [CrossRef]
55. Lee, S.-W.; Choi, B.I.; Woo, S.-B.; Kim, J.C.; Kim, Y.-G. Calibration of a radiosonde humidity sensor at low temperature and low pressure. *Metrologia* **2019**, *56*, 5. [CrossRef]
56. Smith, R.N.B. A scheme for predicting layer clouds and their water content in a general circulation model. *Q. J. R. Meteorol. Soc.* **1990**, *116*, 435–460. [CrossRef]